
Since January 2020 Elsevier has created a COVID-19 resource centre with free information in English and Mandarin on the novel coronavirus COVID-19. The COVID-19 resource centre is hosted on Elsevier Connect, the company's public news and information website.

European Journal of Medicinal Chemistry 251 (2023) 115226

Contents lists available at ScienceDirect

European Journal of Medicinal Chemistry

journal homepage: www.elsevier.com/locate/ejmech

Research paper

# Korupensamine A, but not its atropisomer, korupensamine B, inhibits SARS-CoV-2 *in vitro* by targeting its main protease ($M^{pro}$)

Ahmed M. Sayed [a], Alyaa Hatem Ibrahim [b], Nasir Tajuddeen [c], Jürgen Seibel [d], Jochen Bodem [e], Nina Geiger [e], Kathrin Striffler [e], Gerhard Bringmann [d,*], Usama Ramadan Abdelmohsen [f,g,**]

[a] Department of Pharmacognosy, Faculty of Pharmacy, Nahda University, Beni-Suef, 62513, Egypt
[b] Department of Pharmacognosy, Faculty of Pharmacy, Sohag University, Sohag, 82524, Egypt
[c] Department of Chemistry, Ahmadu Bello University, 15 Sokoto Road Samaru, Zaria, 810107, Nigeria
[d] Institute of Organic Chemistry, University of Würzburg, Am Hubland, 97074, Würzburg, Germany
[e] Institute of Virology and Immunobiology, University of Würzburg, Versbacher Str. 7, 97078, Würzburg, Germany
[f] Department of Pharmacognosy, Faculty of Pharmacy, Minia University, Minia, 61519, Egypt
[g] Department of Pharmacognosy, Faculty of Pharmacy, Deraya University, Universities Zone, New Minia City, 61111, Egypt

ARTICLE INFO

*Keywords:*
Alkaloids
Natural products
Naphthylisoquinolines
SARS-CoV-2
$M^{pro}$
Steered molecular dynamics

ABSTRACT

By combining docking and molecular dynamics simulations, we explored a library of 65 mostly axially chiral naphthylisoquinoline alkaloids and their analogues, with most different molecular architectures and structural analogues, for their activity against SARS-CoV-2. Although natural biaryls are often regarded without consideration of their axial chirality, they can bind to protein targets in an atroposelective manner. By combining docking results with steered molecular dynamics simulations, we identified one alkaloid, korupensamine A, that atropisomer-specifically inhibited the main protease ($M^{pro}$) activity of SARS-CoV-2 significantly in comparison to the reference covalent inhibitor GC376 ($IC_{50}$ = 2.52 ± 0.14 and 0.88 ± 0.15 μM, respectively) and reduced viral growth by five orders of magnitude *in vitro* ($EC_{50}$ = 4.23 ± 1.31 μM). To investigate the binding pathway and mode of interaction of korupensamine A within the active site of the protease, we utilized Gaussian accelerated molecular dynamics simulations, which reproduced the docking pose of korupensamine A inside the active site of the enzyme. The study presents naphthylisoquinoline alkaloids as a new class of potential anti-COVID-19 agents.

## 1. Introduction

Since the first identified cases of the greatly contagious coronavirus disease 2019 (COVID-19) in December 2019, the world has been facing a critical fight against this newly discovered disease, with more than 622 million diagnosed cases and more than 6.5 million deaths up till November 2022 [1,2]. The COVID-19 pandemic is caused by the novel severe acute respiratory syndrome coronavirus 2 (SARS-CoV-2) [3], triggering an acute disease that can eventually result in respiratory failure and death [4]. The SARS-CoV-2 infection has a high transmission rate but a relatively low death rate (1.0–3.5%), except for older people with other comorbidities. Severe pneumonia is observed in 15–20% of the infected people, and 5–10% of the patients require critical-care services [5,6]. SARS-CoV-2 is characterized by a spherical morphology with spike projections on its surface. The spike glycoprotein of the virus controls its entry into the human host cell [7]. SARS-CoV-2 infects lung type II alveolar cells, which may explain the severe alveolar damage during the infection [8]. Although a number of vaccines against SARS-CoV-2 have been successfully developed and administered [9,10], the world is still lacking an effective antiviral treatment against the disease [11].

Medical drugs currently in use are, so far, remdesivir, an antiviral agent that demonstrated benefits in decreasing the rate and the duration of hospitalization [12,13], and dexamethasone, a broad-spectrum anti-inflammatory drug offering assistance to patients with respiratory failure requiring respiratory support through the inhibition of a cytokine storm [14,15]. Also, nirmatrelvir, an orally active 3C-like protease inhibitor in combination with ritonavir, also known as paxlovid, is an antiviral drug against COVID-19 [16].

SARS-CoV-2 contains several polypeptides that promote proteolytic

* Corresponding author. Institute of Organic Chemistry, University of Würzburg, Am Hubland, 97074, Würzburg, Germany.
** Corresponding author. Department of Pharmacognosy, Faculty of Pharmacy, Deraya University, Universities Zone, New Minia City, 61111, Egypt.
*E-mail addresses:* bringman@chemie.uni-wuerzburg.de (G. Bringmann), usama.ramadan@mu.edu.eg (U.R. Abdelmohsen).

https://doi.org/10.1016/j.ejmech.2023.115226
Received 5 December 2022; Received in revised form 7 February 2023; Accepted 20 February 2023
Available online 28 February 2023

breakdown to produce 20 additional proteins during their lifecycle; one of them is the main protease ($M^{pro}$), which is essential for virus replication [17]. It consists of 306 amino acid residues and resembles the $M^{pro}$ of SARS-CoV in structure and sequence [11,18,19]. This essential protease is a dimer, and mutations that prevent its conserved dimerization greatly reduce its catalytic activity. There are three domains in each monomer (domains I-III), of which domains I and II form the catalytic binding pocket, and domain III is responsible for enzyme dimerization [20,21]. The functional $M^{pro}$ must have a conserved HIS-41-CYS-145 catalytic dyad in its active site. As a result, the catalytic activity of the enzyme will degenerate to the point where it is no longer functional if these catalytic residues are altered [22]. Several non-competitive inhibitors have been reported to form covalent bonds with CYS-145 like e.g., nirmatrelvir, ensiltrelvir, narlaprevir, and boceprevir, but there has been much less research into competitive non-covalent inhibitors [23,24]. Therefore, efforts have focused on investigating the main protease of that virus, to discover new specific non-covalent inhibitors against COVID-19 [7,25]. For more details on the discovery of inhibitors of various SARS-CoV-2 proteins, including $M^{pro}$, see Refs. [26–28].

A particularly interesting – and stereochemically intriguing – group of natural products are the naphthylisoquinoline (NIQ) alkaloids like korupensamine A (**1a**, see Fig. 1) [29]. They are composed of a naphthalene and an isoquinoline moiety. Following the principle of phenol-oxidative coupling, the two molecular portions are joined together in different ways, always *ortho* or *para* to oxygen functions [30,31]. These coupling types determine the molecular shapes of the alkaloids; Fig. 1 shows a selection of differently coupled NIQs, with representatives linked *via* the 5,8′-positions (like in compounds **1a**/**1b**-**4**), *via* 5,1' (NIQs **5**, **6**, and *ent*-**6**), 7,8' (compound **7**), or 7,1' (alkaloids **8** and **9**). NIQ alkaloids are chiral compounds, characterized by the presence of stereogenic centers and a usually likewise chiral *C*,*C*- or *N*,*C*-axis between the two molecular moieties, the isoquinoline and the naphthalene portions. Due to the existence of more or less bulky *ortho*-substituents, most of these alkaloids show the phenomenon of hindered rotation about that central biaryl axis, which – in most cases - leads to rotationally stable atropisomers [30–33]. Atropisomerism as an important structural feature of these alkaloids constitutes a synthetic challenge for their directed, stereoselective production that has been addressed in numerous elegant total syntheses [34,35]. One motivation for these synthetic efforts is the fact that, depending on their individual structures, naphthylisoquinoline alkaloids exhibit pronounced anti-malarial [32,36–39], anti-trypanosomal [30,32,40], anti-leishmanial [31,32,40–43], anti-bacterial [32,44], anti-fungal [32], larvicidal [45], molluscicidal [46,47], insecticidal [48,49], antibabesial [50], or cytotoxic activities against leukemia [51] and various cancer cell lines [52–55]. Moreover, some dimeric naphthylisoquinolines, like michellamine B [56] (for the structure, see Table S1), show potent antiviral activities; they display anti-HIV effects by inhibition of certain viral enzymes like, for instance, reverse transcriptases (RTs) of both HIV type 1 and 2, as well as human alpha and beta DNA polymerases. Additionally, they can interfere with the late stages of the virus replication cycle by inhibiting cellular fusion and syncytium formation [56–59].

Scientists have embarked on developing an effective and safe treatment for COVID-19 [26], which stimulated us to conduct the present study to search for new drug leads against SARS-CoV-2 infection. In this paper, we describe the first investigation of a library of structurally most different mono- and dimeric NIQ alkaloids and selected structural analogues for their activity against SARS-CoV-2. Additionally, we investigated an integrated docking-MDS (molecular dynamics simulations) approach for speeding up and improving the selection of potentially active compounds among a group of closely related structures.

## 2. Results and discussion

### 2.1. General approach

In the frame of our continued search for potential anti-SARS-CoV-2 therapeutics [21,60–64], we investigated a small library of bioactive NIQs in the quest for inhibitors of the $M^{pro}$ of SARS-CoV-2. Most of the compounds of this library (53 out of 65 structures) are atropisomerically well-defined biaryls (Table S1). Since atropisomers are stereoisomers resulting from impeded rotation about a single bond, their structures are intrinsically less flexible than those of the corresponding freely rotating conformers, and hence they are of lower entropy. Drugs with lower entropy are likely to have a higher affinity for receptors and enzymes, as the binding process will result in less loss of entropy. From this point, we started a molecular docking-based screening of the NIQ library against the structure of the $M^{pro}$ of SARS-CoV-2 to find possible binders and, thus, potential inhibitors.

### 2.2. Docking-based screening

At the beginning of the docking step, we validated the docking protocol by AutoDock Vina [65], re-docking the co-crystallized ligands of two previously reported [66,67] SARS-CoV-2 $M^{pro}$ structures (PDB ID: 7DPP and 7LTJ). The resulting top-scoring docking poses of these inhibitors aligned with the co-crystallized ones with acceptable root-mean-square deviation (RMSD) values of 1.26 Å and 0.89 Å, respectively.

The modeled structures of the compounds of the library were prepared and docked into the active site of $M^{pro}$ using the AutoDock Vina software [65]. Since all of the compounds in the used library contained basic - secondary or tertiary - amino functions, we also investigated the protonated forms of the compounds for the docking step. AutoDock Vina does not take steric hindrance into consideration during the docking process, where it makes the structures of the molecules free to rotate independently of the energetics of the whole molecules. For this reason, the resulting poses for each structure in the library were filtered according to the correct and low-energy conformations. A binding score of −7 kcal/mol was another filter criterion for selection, according to which the structures and poses of lower scores were neglected.

As a result, 11 out of the 65 initially considered structures were selected as top candidates for the subsequent *in silico* and *in vitro* testing (Figs. 1 and 2A). It is worth noting that all generated poses for each of the top-scoring structures had almost the same binding mode. They aligned perfectly with each other, with a low RMSD value of 0.947 Å. This observation can be attributed to the low flexibility of the docked structures, where the number of available conformations that can generate different poses was limited. Such a uniformity of the docking poses indicated that the top-ranked pose of each docked structure was likely to be the correct one. However, further refinement, based on molecular dynamics simulation, was required, particularly the calculation of $\Delta G_{binding}$ for each generated pose. This docking-based step managed to filter out ancistrocladine (docking score = −6.7 kcal/mol; for the structure, see Table S1) from its atropisomer, hamatine (**6**) (−8.2 kcal/mol), while it was not able to discriminate between the atropodiastereomeric alkaloids korupensamine A (**1a**) and korupensamine B (**1b**), where both structures got the same score (−7.9 kcal/mol).

### 2.3. $\Delta G_{binding}$-based refinement

Using the alchemical Free Energy Perturbation (FEP) method [68], we then determined the $\Delta G_{binding}$ for the top candidates. By this procedure, $\Delta G_{binding}$ values were extracted by running a series of MDS experiments. The 11 selected structures (Fig. 1) exhibited $\Delta G_{binding}$ values ranging from −5.38 to −8.85 kcal/mol (Figs. 1 and 2B), indicating good affinities towards the active site of $M^{pro}$ and, in turn, potential antiviral activity against SARSCoV-2. Based on the binding affinity values, it was

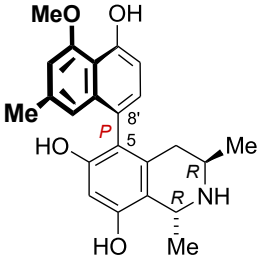

Korupensamine A (**1a**)
Docking score = -7.9 kcal/mol
$\Delta G_{binding}$ = -8.57 kcal/mol

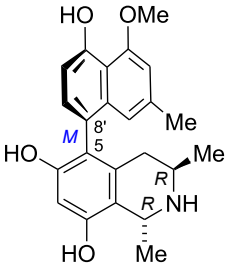

Korupensamine B (**1b**)
Docking score = -7.9 kcal/mol
$\Delta G_{binding}$ = -7.04 kcal/mol

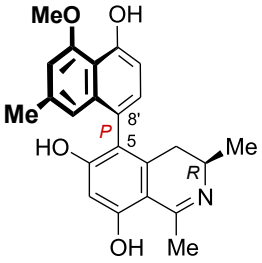

Ancistrolikokine E (**2**)
Docking score = -7.7 kcal/mol
$\Delta G_{binding}$ = -5.38 kcal/mol

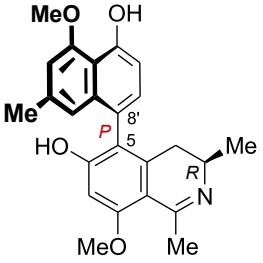

Ancistrolikokine $E_2$ (**3**)
Docking score = -7.5 kcal/mol
$\Delta G_{binding}$ = -8.16 kcal/mol

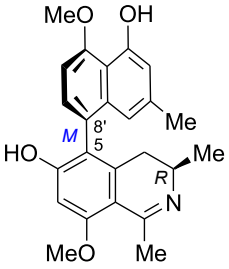

Ancistrolikokine F (**4**)
Docking score = -7.4 kcal/mol
$\Delta G_{binding}$ = -7.18 kcal/mol

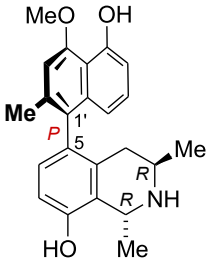

Dioncophylline C (**5**)
Docking score = -7.9 kcal/mol
$\Delta G_{binding}$ = -8.85 kcal/mol

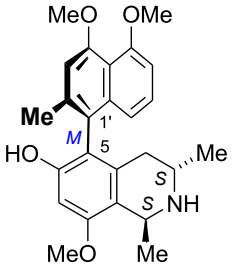

Hamatine (**6**)
Docking score = -8.2 kcal/mol
$\Delta G_{binding}$ = -7.23 kcal/mol

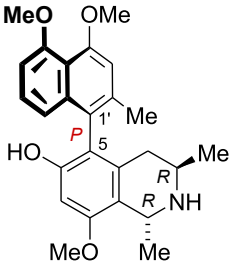

*ent*-Hamatine (*ent*-**6**)
Docking score = -7.7 kcal/mol
$\Delta G_{binding}$ = -8.67 kcal/mol

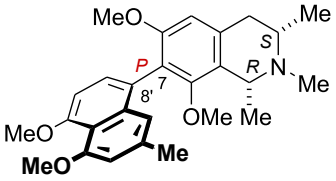

Ancistrobrevine A (**7**)
Docking score = -7.5 kcal/mol
$\Delta G_{binding}$ = -7.95 kcal/mol

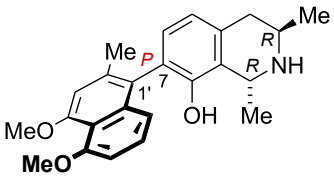

Dioncophylline A (**8**)
Docking score = -7.1 kcal/mol
$\Delta G_{binding}$ = -6.47 kcal/mol

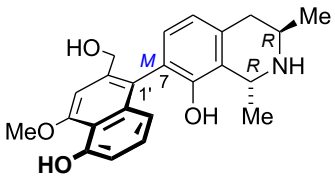

Dioncopeltine A (**9**)
Docking score = -7.5 kcal/mol
$\Delta G_{binding}$ = -7.87 kcal/mol

**Fig. 1.** Structures of the eleven out of 65 selected top-scoring compounds with different molecular shapes retrieved from the docking step, among them 5,8′-coupled alkaloids (compounds **1a**/**1b**-**4**) as well as representatives with 5,1'- (**5**, **6**, and *ent*-**6**), 7,8'- (**7**), or 7,1′-axes (**8**, **9**).

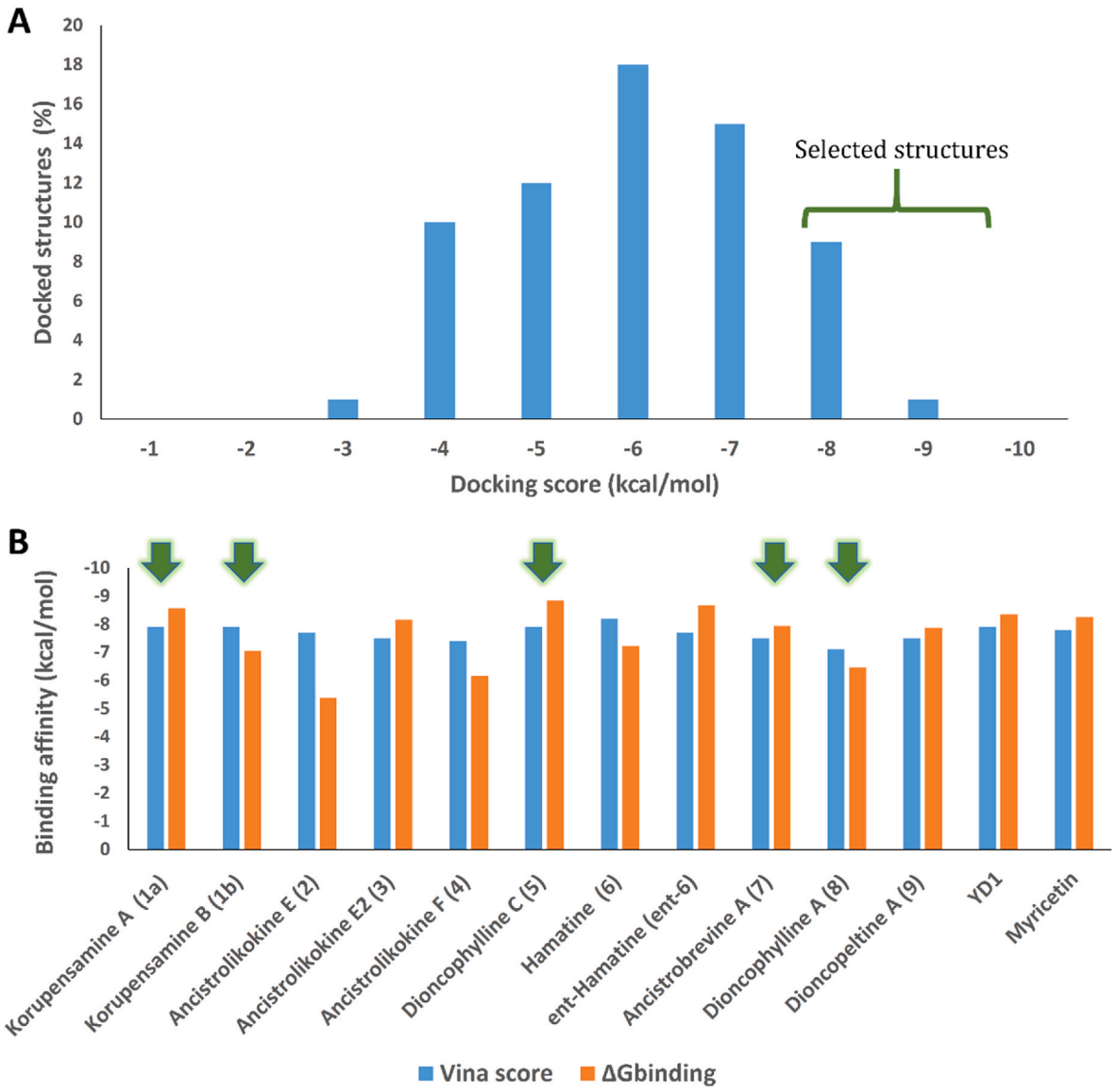


**Fig. 2.** (A) Score distribution of the docked structures in the NIQ library against the $M^{pro}$ of SARS-CoV-2. Structures with docking scores < -7 kcal/mol (17.5%) were selected for validation by MDS and $\Delta G_{binding}$ calculation. (B) Docking scores in comparison with the $\Delta G_{binding}$ values of the top-scoring compounds selected from the docking step, along with those of the co-crystallized inhibitors YD1 and myricetin. Green arrows indicate compounds that were selected for *in vitro* antiviral testing.

hard to discriminate between these selected structures regarding their potential activity. Moreover, the two atropo-diastereomeric alkaloids korupensamine A (**1a**) and korupensamine B (**1b**), possessing the same gross structure, showed no significant difference in the calculated $\Delta G_{binding}$ values ($\Delta\Delta G_{binding} = -1.5$ kcal/mol, see Fig. 1). Such a minor difference was not large enough to prefer one atropisomer over the other. This was not the case with the second pair of atropisomers investigated, ancistrocladine (for the structure, see Table S1) and hamatine (**6**), whose calculated $\Delta G_{binding}$ values were significantly different (−3.88 kcal/mol and −7.23 kcal/mol, respectively; hence $\Delta\Delta G_{binding} = -3.35$ kcal/mol).

### 2.4. Steered molecular dynamics simulation

For this reason, we present herein the advantage of using steered molecular dynamics (SMD) in the discrimination between related congeners in terms of their affinity towards the active site of $M^{pro}$, by the determination of their relative binding affinity.

To do so, the top-ranked docking poses for each structure of the previously selected 11 compounds alongside the co-crystallized inhibitors (myricetin and YD1) were prepared and subjected to a number of SMD runs, where an external force was applied to each structure to pull it out of the $M^{pro}$ active pocket, and hence, these applied forces can be traced over the course of the steering simulation.

Remarkably, the force needed to unbind korupensamine A (compound **1a**, 1283 pN) was comparable to those needed to unbind the previously reported co-crystallized inhibitors myricetin and YD (1522 pN and 1323 pN, respectively). In addition, their steering force profiles clustered together away from those of all of the remaining structures, including the structurally so closely related korupensamine B (**1b**). The unbinding forces of those other structures did not exceed 480 pN (Fig. 3A and B).

### 2.5. Atropo-selective $M^{pro}$ inhibitory activity of korupensamine A (*1a*) in vitro

*In vitro* validation on the $M^{pro}$ activity assay supported these findings (Fig. 4), where korupensamine A (**1a**) suppressed the catalytic activity of the enzyme in a dose-dependent manner, with an $IC_{50}$ value of 2.53 ± 0.138 μM ($K_i$ = 1.42 ± 0.12 μM), while its atropo-diastereomer,

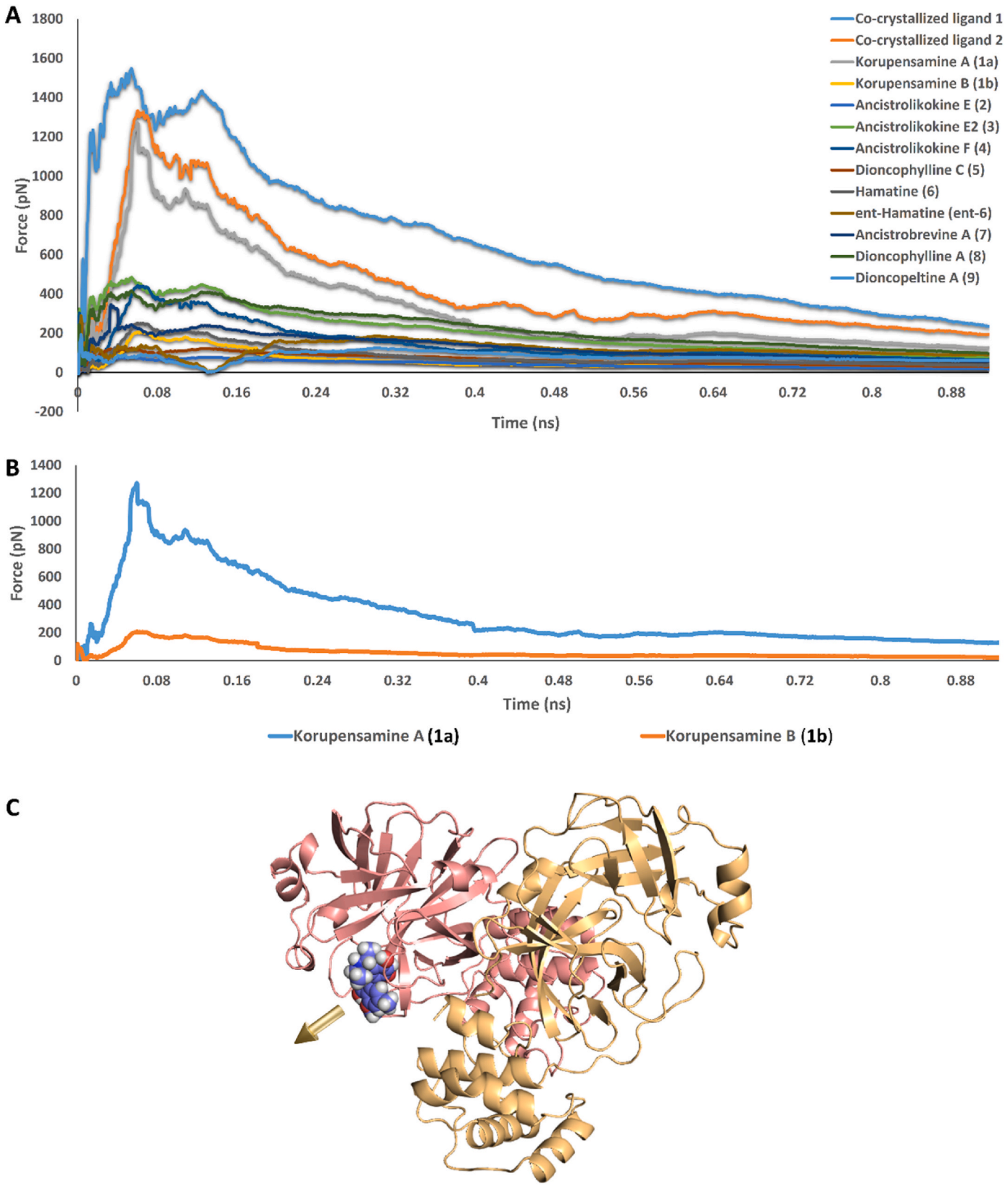


**Fig. 3.** (A) Comparison of the unbinding force profiles of the selected 11 structures shown in Fig. 1, alongside that of the co-crystallized inhibitors (myricetin and YD1; co-crystallized ligands 1 and 2, respectively). The plots show the resulting mean values from averaging the force profiles from three different SMD runs ($n = 3$) for each structure. (B) Unbinding force profiles of korupensamine A (**1a**) *versus* its atropisomer korupensamine B (**1b**), showing the significant difference in the relative affinity of the two structures toward the active site of $M^{pro}$. (C) The golden-yellow arrow indicates the pulling direction for the ligand-unbinding pathway.

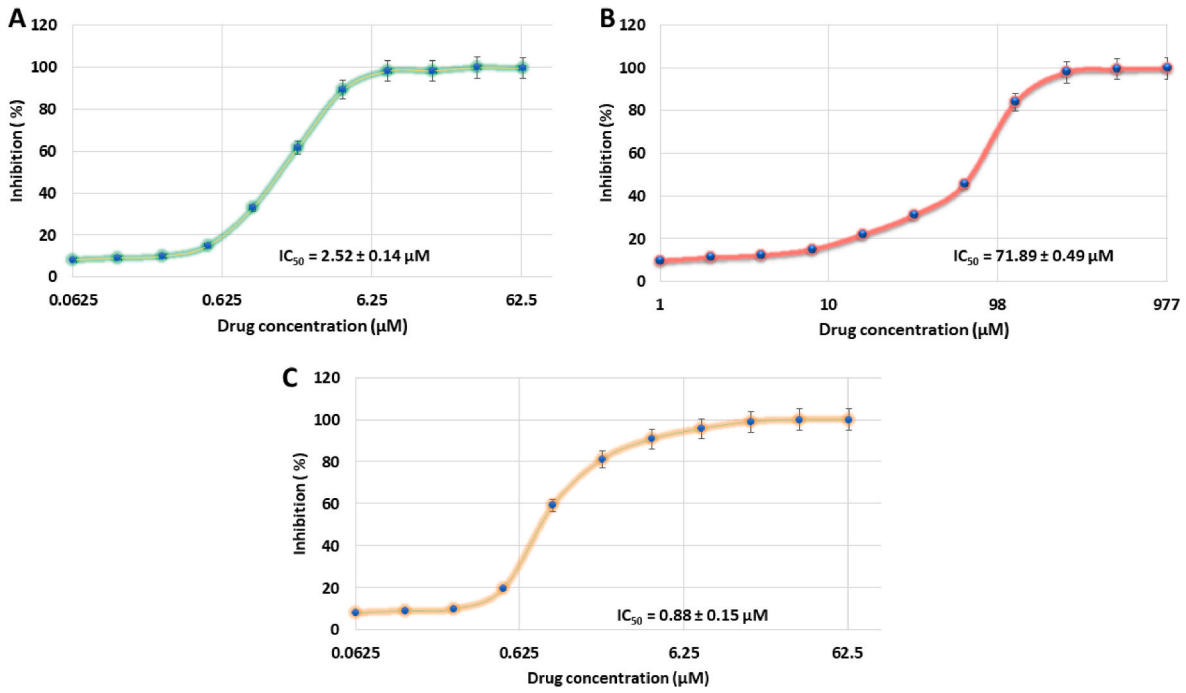


**Fig. 4.** Inhibition of the activity of the SARS-CoV-2 $M^{pro}$ by korupensamine A (**1a**) and korupensamine B (**1b**) at increasing concentrations of the inhibitor. The enzyme activity is reduced by 50% at a korupensamine A (**1a**) concentration of 2.52 ± 0.14 µM (A) in comparison to that of korupensamine B (**1b**) at a concentration of 71.89 ± 0.49 µM (B) and that of the reference inhibitor GC376 [70] at a concentration of 0.88 ± 0.15 µM (C).

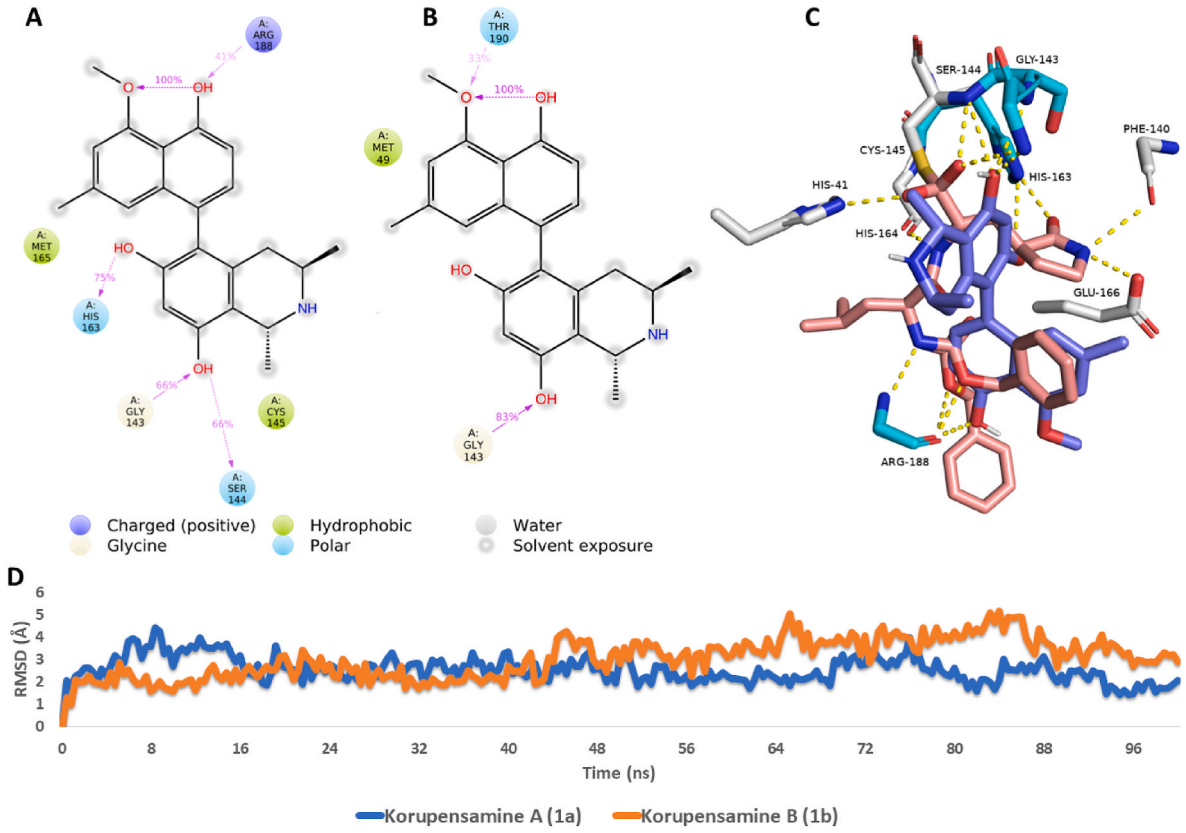


**Fig. 5.** Ligand-protein interactions extracted from the 100-ns long MDS experiments of (A) korupensamine A (**1a**) and (B) korupensamine B (**1b**). 3D binding mode of korupensamine A (**1a**, in blue) in alignment with the reference inhibitor GC376 (brick-red structures) inside the active site of $M^{pro}$ (C). The cyan-colored amino acid residues interact with both structures (i.e., korupensamine A and GC376), while white-colored amino acid residues interact with GC376 only. RMSDs of korupensamines A (**1a**) and B (**1b**) over the course of their MDS runs (D). Colored arrows in (A) and (B) indicate the percentage of interaction with each amino acid residue during the MDS runs.

korupensamine B (**1b**), i.e., with the same constitution as **1a**, and possessing the same absolute configuration at both stereocenters, differing only by the axial configuration, was inactive up to 50 μM ($IC_{50}$ = 71.89 ± 0.49 μM).

These enzyme inhibitory results clearly showed the superior affinity of korupensamine A (**1a**) over its atropisomer korupensamine B (**1b**) – and over all of the other remaining compounds. This result emphasized, once again, the impact of axial chirality for the bioactivity of rotationally hindered biaryl agents in general, and in this particular case, the pronounced structure-specificity of the inhibitory activity of korupensamine A (**1a**). Additionally, the results highlighted the efficacy of the SMD approach in the differentiation between atropisomers in terms of their biomolecular interactions.

SMD had previously been reported to be an effective method of discerning between flavonoids in terms of their enzyme inhibition activity [69]. Here, once again, this fast and reliable *in silico* method proved its ability in pointing out the active anti-SARS-CoV-2 representative among a group of structurally most similar potential candidates.

### 2.6. Dynamic mode of interaction

To get some insight into the dynamic binding interactions of korupensamine A (**1a**) inside the active site of $M^{pro}$ in comparison to those of its atropo-diastereomer (i.e., korupensamine B, **1b**), the selected poses of both compounds were subjected to 100-ns MDS runs. The dynamic interactions of the two structures were then extracted and analyzed (see Fig. 5). As shown in Fig. 5D, the binding stability of the two compounds inside the active site of the enzyme was comparable to an average RMSDs of 2.43 Å and 3.72 Å for korupensamines A (**1a**) and B (**1b**), respectively. On the one hand, both structures formed stable H-bonds with GLY-143 over the course of the simulation (Fig. 5A and B), but, on the other hand, only korupensamine A (**1a**) formed three additional stable H-bonds with SER-144, HIS-163, and ARG-188, while only korupensamine B (**1b**) established another single H-bond with THR-190. Moreover, korupensamine A (**1a**) had stable hydrophobic interactions with MET-165 and CYS-145, while korupensamine B (**1b**) revealed a single stable hydrophobic interaction with MET-49. Accordingly, korupensamine A (**1a**) exhibited thermodynamically more stable interactions inside the $M^{pro}$ active site than its atropisomer, korupensamine B (**1b**). This explains why much more force was required to steer **1a** out of the active site of the enzyme than the one needed in the case of **1b** (Fig. 3B). Alignment of the structure of korupensamine A (**1a**) with that of the reference inhibitor GC376 (Fig. 5C) indicated that both structures have four common hydrophilic interactions (i.e., H-bonds) with GLY-143, SER-144, HIS-163, and ARG-188. Accordingly, H-bonding to these residues might be essential for good binding and inhibition of the $M^{pro}$ of SARS CoV-2.

### 2.7. Gaussian accelerated molecular dynamics (GaMD) simulations

In order to explore the binding pathway of korupensamine A (**1a**) to the active site of $M^{pro}$, three independent Gaussian accelerated molecular dynamics simulations (GaMD) were carried out. In each 400-ns long simulation, five replicates of the structure of korupensamine A (**1a**) were placed in the solvent box at least 20 Å away from the modeled $M^{pro}$ structure. In one of the three simulations, ligand binding was observed after 115.92 ns and remained stable inside the $M^{pro}$ active site until the end of the simulation (Fig. 6A). Interestingly, the final binding state (Fig. 6B) was almost identical to that of the top-scoring docking pose selected earlier (RMSD = 1.63 Å), indicating that this binding pose is the most likely one.

Additionally, the four amino acid residues that had earlier been found to interact with korupensamine A (**1a**) *via* H-bonding (GLY-143, SER-144, HIS-163, and ARG-188) were also the interacting ones upon korupensamine A binding.

### 2.8. Korupensamine A (*1a*) inhibits SARS-CoV-2 in cell culture

Due to a quantity limitation, we selected five out of the top potentially active 11 alkaloids (Figs. 1 and 2B), along with another three compounds predicted to be inactive - the dimeric alkaloids michellamine A, which is the 6′,6″-dimer of korupensamine A (**1a**), michellamine B, i.e. the mixed dimer of korupensamines A (**1a**) and B (**1b**), and plumbagin, the oxidized naphthalene part of the presented NIQs (for the structures, see Table S1) - for *in vitro* antiviral testing against SARS-CoV-2. Surprisingly, only korupensamine A (**1a**) was active against SARS-CoV-2, it reduced the viral replication at 30 μM by five orders of magnitude ($EC_{50}$ = 4.23 ± 1.31 μM; $CC_{50}$ = 35.1 μM) (Fig. S2). From this observation it can be concluded that docking and $\Delta G_{binding}$ calculation were good in predicting active compounds, but not sufficient to discriminate between compounds of convergent scores and between atropisomers, here korupensamine A (**1a**) *versus* korupensamine B (**1b**), whereas SMD demonstrated its efficacy in identifying the one anti-SARS-CoV-2 agent from of a pool of structurally similar compounds.

## 3. Conclusion

Understanding the interactions between ligands and proteins is essential for a rational structure-based drug design. In this work, several methods combining docking and MDS (molecular docking simulations) have been utilized to investigate the mode of interaction of pharmaceutically relevant complexes in the field of axially chiral naphthylisoquinoline (NIQ) alkaloids and their analogues. To identify potential ligands for the SARS-CoV-2 $M^{pro}$, we used docking-based virtual screening in conjunction with $\Delta G_{binding}$ calculations to examine a library of 65 structures of such alkaloids.

The top-scoring structures were subjected to binding free energy and SMD experiments to determine their relative affinity towards the active site of the enzyme and hence, distinguishing the most probably active candidate, korupensamine A (**1a**). Upon *in vitro* validation, **1a** was found to be the only actual $M^{pro}$ inhibitor, possessing an $IC_{50}$ value of 2.52 μM, with significant antiviral activity against SARS-CoV-2, comparable to that of the reference inhibitor GC376 ($IC_{50}$ = 0.88 μM). Accordingly, from a collection of structurally related, atropisomerically defined NIQ

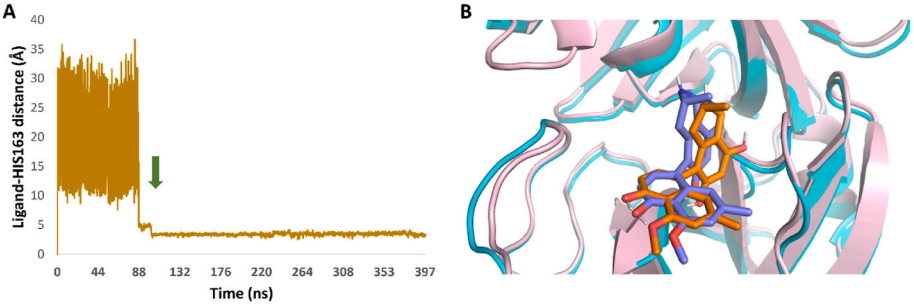


**Fig. 6.** (A) Binding event of korupensamine A (**1a**) with the $M^{pro}$ active site observed in GaMD simulation after 115.92 ns (the green arrow indicates the beginning of the binding event). (B) Structure alignment of the docking pose of korupensamine A (**1a**, orange structure) on its most populated structure after its binding inside the active site of $M^{pro}$ during the GaMD simulation (blue structure). RMSD value between the two states = 1.63 Å. A video showing the binding event of korupensamine A (**1a**) inside the active site of $M^{pro}$ can be found on the Zenodo website: https://zenodo.org/record/7312007#.Y35sVXbP2M9.

alkaloids, SMD simulation was found to be a fast and accurate method for predicting the best $M^{pro}$ inhibitor.

Finally, using Gaussian accelerated molecular dynamics (GaMD) simulations over 400 ns, we explored the binding pathway and the mode of recognition and interaction of korupensamine A (**1a**) within the active site of $M^{pro}$.

Intriguingly, GaMD simulations managed to simulate the binding process of korupensamine A (**1a**) and to reproduce its docking position within the active site of the enzyme, demonstrating the validity of our approach from the outset. The study shows that using computational chemistry methods helps the drug discovery process move forward. Our strategy presented here could effectively supplement commonly used docking simulations, especially when there are only minor structural differences within a series of analogues, where docking studies may have failed to properly rank the binding affinities.

The work furthermore reveals naphthylisoquinoline alkaloids as a highly promising new class of potential anti-SARS-CoV-2 agents. The highlight among these axially chiral alkaloids is korupensamine A (**1a**), which does not only bind strongly to the main protease of the virus *in silico*, but is also active *in vitro*, with a high structure specificity: All of the numerous other alkaloids, whether ring-opened, ring-contracted or quinoid, as well as their non-coupled isoquinoline and naphthalene moieties (see Table S1), were inactive, also the respective dimers, even including the closely related korupensamine B (**1b**), which differs from **1a** only by the configuration at the rotationally hindered biaryl axis. This pinpoints, once again, the importance of axially chirality, which dictates the molecular shape of a bioactive compound, and thus, determines its bioactivity.

## 4. Experimental

### 4.1. Naphthylisoquinoline alkaloids and related compounds

The NIQs experimentally investigated in the present study and their analogues were prepared by isolation from their plant sources [56, 71–76] or by total synthesis [77], as described previously (for further details, see Table S1), and have been deposited in our in-house natural products library.

### 4.2. Molecular docking

#### 4.2.1. Structure generation

The structures of the NIQs and their analogues used in the present study were generated using ChemDraw (12.0). Their rotational-energy profiles were calculated after energy minimization using Chem3D (12.0).

#### 4.2.2. Ligand preparation

All torsions of the collected structures were assigned and their Gasteiger charges were added for all atoms in the compound structures using the AutoDockTools v.4.2 package [78].

#### 4.2.3. Receptor preparation

For docking screening, the $M^{pro}$ structures with the co-crystallized ligands myricetin and YD1 (PDB codes: 7DPP and 7LTJ, respectively) were used. The downloaded structures were curated on PDBfixer [79] to repair lost atoms and residues, and for removing co-crystallized water molecules. Polar hydrogens and Gasteiger charges were then added to all receptor structures using AutoDockTools v.4.2 [78].

#### 4.2.4. Structural docking

For the docking step, AutoDock Vina software integrated in the PyRx platform was used [80,81]. The binding site for the docking search was determined according to the co-crystallized ligand of the enzyme, 6G9. The coordinates of the grid box were: x = −7.58; y = 16.39; z = 2.44. The size of the grid box was set to be 10 $Å^3$ (for small structures) and 20 $Å^3$ (for larger structures). Exhaustiveness was set to be 24. Docking poses were analyzed and visualized using the PyMOL software [80]. The docking protocol was validated by re-docking the co-crystallized inhibitor (6G9). The resulting top-scoring pose (score = −7.12 kcal/mol) was found to achieve a good alignment with the original co-crystallizing pose, with a low RMSD value (1.26 Å). After docking the structures of the NIQ library, a cut-off value of −7.0 kcal/mol was set to select the best ligands. This cut-off value was set according to the lowest docking score of the co-crystallized ligands (6G9 and myricetin), which got scores of −7.12 and −8.82 kcal/mol, respectively.

### 4.3. Molecular dynamics and $\Delta G_{binding}$ determination

Molecular dynamics simulations (including SMD) and binding free energy determination were carried out as described earlier [82]. GaMD simulations were performed according to the previously reported method of Miao and co-workers [83]. The detailed procedures are described in the Supplementary data.

### 4.4. $M^{pro}$ enzyme assay (in vitro)

Top-scoring compounds were assessed for their *in vitro* enzyme inhibition activities using 3CL Protease, tagged (SARS-CoV-2) Assay Kit (Catalogue #: 79955-1, BPS Bioscience, Inc., Allentown, PA, USA), according to manufacturer's protocol [5]. The *in vitro* FRET assay was monitored at an emission wavelength of 460 nm with an excitation at 360 nm, using a Flx800 fluorescence spectrophotometer (BioTek Instruments, Winooski, VT, USA).

### 4.5. In vitro antiviral assay

Vero cells were incubated with the compounds for 3 days to investigate cytotoxicity, and the relative cell growth was determined by automatic cell counting. Concentrations of 30 μM of **1a** and **1b** did not influence cell growth. The Vero cells were then incubated with the respective compounds at increasing concentrations and subsequently infected with patient-derived SARS-CoV-2 at an MOI (Multiplicity of Infection) of approximately 0.5. DMSO was used as a solvent control [84]. After 24 h, the medium was replaced by compound-containing medium, to remove inactive viruses. After 3 days, viral replication supernatants were collected, and viral RNA was extracted. Viral replication was quantified by real-time RTqPCR. All infections were performed in triplicate [84,85].

## Declaration of competing interest

The authors declare that they have no known competing financial interests or personal relationships that could have appeared to influence the work reported in this paper.

## Data availability

Data will be made available on request.

## Acknowledgements

This work was supported by Deraya University and the University of Würzburg. The authors thank Dr. D. Feineis and Prof. C. Sotriffer for valuable advice, and Dr. W. Shamburger for initial help with the structures.

## Appendix A. Supplementary data

Supplementary data to this article can be found online at https://doi.org/10.1016/j.ejmech.2023.115226.

## Abbreviations

| | |
|---|---|
| cMD | Classical Molecular Dynamics |
| DMSO | Dimethyl Sulfoxide |
| FEP | Free Energy Perturbation |
| FF14SB | Force Field 14 Stony Brook |
| $\Delta G_{binding}$ | Absolute Binding Free Energy |
| GaMD | Gaussian Accelerated Molecular Dynamics |
| GPUs | Graphics Processing Unit |
| GUI | Graphical User Interface |
| $IC_{50}$ | Half Maximal Inhibitory Concentration |
| $K_i$ | Inhibitor Constant |
| MDS | Molecular Dynamics Simulation |
| MOI | Multiplicity of Infection |
| $M^{pro}$ | Main Protease |
| NAMD | Nanoscale Molecular Dynamics |
| NIQ | Naphthylisoquinoline |
| NPT | Constant Pressure and Temperature |
| OPLS | Optimized Potentials for Liquid Simulations |
| PCR | Polymerase Chain Reaction |
| PDB | Protein Data Bank |
| PME | Particle Mesh Ewald |
| pN | Piconewton |
| RMSD | Root-Mean-Square Deviation |
| RMSF | Root-Mean-Square Fluctuation |
| RT | Reverse Transcriptase |
| RTqPCR | Quantitative Reverse Transcription Polymerase Chain Reaction |
| SARS-CoV-2 | Severe Acute Respiratory Syndrome Coronavirus-2 |
| SHAKE | Secure Hash Algorithm Keccak |
| SMD | Steered Molecular Dynamics |
| TIP3P | Transferable Intermolecular Potential with 3 Points |
| VMD | Visual Molecular Dynamics |

## References


[1] O.J. Watson, G. Barnsley, J. Toor, A.B. Hogan, P. Winskill, A.C. Ghani, Global impact of the first year of COVID-19 vaccination: a mathematical modelling study, Lancet Infect. Dis. 22 (2022) 1293–1302.

[2] A. Maxmen, Wuhan market was epicentre of pandemic's start, studies suggest, Nature 603 (2022) 15–16.

[3] M.M. Lamers, B.L. Haagmans, SARS-CoV-2 pathogenesis, Nat. Rev. Microbiol. 20 (2022) 270–284.

[4] D.M.G. Halpin, R. Faner, O. Sibila, J.R. Badia, A. Agusti, Do chronic respiratory diseases or their treatment affect the risk of SARS-CoV-2 infection? Lancet Respir. Med. 8 (2020) 436–438.

[5] T. Liu, E. Siegel, D. Shen, Deep learning and medical image analysis for COVID-19 diagnosis and prediction, Annu. Rev. Biomed. Eng. 24 (2022) 179–201.

[6] A.V. Ballering, S.K.R. van Zon, T. Colde Hartman, J.G.M. Rosmalen, For the Lifelines Corona Research Initiative, Persistence of somatic symptoms after COVID-19 in The Netherlands: an observational cohort study, Lancet 400 (2022) 452–461.

[7] S.A. Amin, S. Banerjee, K. Gosh, S. Gayen, T. Jha, Protease targeted COVID-19 drug discovery and its challenges: insight into viral main protease ($M^{pro}$) and papain-like protease ($PL^{pro}$) inhibitors, Bioorg. Med. Chem. 29 (2021), 115860.

[8] H. Li, Y. Zhou, M. Zhang, H. Wang, Q. Zhao, J. Liu, Updated approaches against SARS-CoV-2, antimicrob, Agents Chemother 64 (2020) e00483-00420.

[9] M. Jeyanathan, S. Afkhami, F. Smaill, M.B.D. Lichty, Z. Xing, Immunological considerations for COVID-19 vaccine strategies, Nat. Rev. Immunol. 20 (2020) 615–632.

[10] S. Machingaidze, C.S. Wiysonge, Understanding COVID-19 vaccine hesitancy, Nat. Med. 27 (2021) 1338–1339.

[11] M. Mei, X. Tan, Current strategies of antiviral drug discovery for COVID-19, Front. Mol. Biosci. 8 (2021), 671263.

[12] J.H. Beigel, K.M. Tomashek, L.E. Dodd, A.K. Mehta, B.S. Zingman, A.C. Kalil, E. Hohmann, H.Y. Chu, A. Luetkemeyer, S. Kline, D. Lopez de Castilla, R. W. Finberg, K. Dierberg, V. Tapson, L. Hsieh, T.F. Patterson, R. Paredes, D. A. Sweeney, W.R. Short, G. Touloumi, D.C. Lye, N. Ohmagari, M. Oh, G.M. Ruiz-Palacios, T. Benfield, G. Fätkenheuer, M.G. Kortepeter, R.L. Atmar, C.B. Creech, J. Lundgren, A.G. Babiker, S. Pett, J.D. Neaton, T.H. Burgess, T. Bonnett, M. Green, M. Makowski, A. Osinusi, S. Nayak, H.C. Lane, For the ACTT-1 study members, remdesivir for the treatment of Covid-19 — final report, N. Engl. J. Med. 383 (2020) 1813–1826.

[13] S.A. Kemp, D.A. Collier, R.P. Datir, I.A. Ferreira, S. Gayed, A. Jahun, M. Hosmillo, C. Rees-Spear, P. Mlcochova, I.U. Lumb, SARS-CoV-2 evolution during treatment of chronic infection, Nature 592 (2021) 277–282.

[14] P.D. Monk, R.J. Marsden, V.J. Tear, J. Brookes, T.N. Batten, M. Mankowski, F. J. Gabbay, D.E. Davies, S.T. Holgate, L.-P. Ho, T. Clark, R. Djukanovic, T.M. A. Wilkinson, On behalf of the Inhaled Interferon Beta COVID-19 Study Group, Safety and efficacy of inhaled nebulised interferon beta-1a (SNG001) for treatment of SARS-CoV-2 infection: a randomised, double-blind, placebo-controlled, phase 2 trial, Lancet Respir. Med. 9 (2021) 196–206.

[15] The RECOVERY Collaborative Group, Dexamethasone in hospitalized patients with Covid-19, N. Engl. J. Med. 384 (2020) 693–704.

[16] A.S. Anderson, P. Caubel, J.M. Rusnak, For the EPIC-HR trial investigators, nirmatrelvir-ritonavir and viral load rebound in Covid-19, N. Engl. J. Med. 387 (2022) 1047–1049.

[17] B. Goyal, D. Goyal, Targeting the dimerization of the main protease of coronaviruses: a potential broad-spectrum therapeutic strategy, ACS Comb. Sci. 22 (2020) 297–305.

[18] H. Yang, J. Yang, A review of the latest research on $M^{pro}$ targeting SARS-COV inhibitors, RSC Med. Chem. 12 (2021) 1026–1036.

[19] J. Qiao, Y.-S. Li, R. Zeng, F.-L. Liu, R.H. Luo, C. Huang, Y.-F. Wang, J. Zhang, B. Quan, C. Shen, X. Mao, X. Liu, W. Sun, W. Yang, X. Ni, K. Wang, L. Xu, Z.-L. Duan, Q.-C. Zou, H.-L. Zhang, W. Qu, Y.H.P. Long, M.-H. Li, R.-C. Yang, X. Liu, J. You, Y. Zhou, R. Yao, W.-P. Li, J.-M. Liu, P. Chen, Y. Liu, G.-F. Lin, X. Yang, J. Zou, L. Li, Y. Hu, G.-W. Lu, W.-M. Li, Y.-Q. Wei, Y.-T. Zheng, J. Lei, S. Yang, SARS-CoV-2 $M^{pro}$ inhibitors with antiviral activity in a transgenic mouse model, Science 371 (2021) 1374–1378.

[20] A. Pavlova, D.L. Lynch, I. Daidone, L. Zanetti-Polzi, M.D. Smith, C. Chipot, D. W. Kneller, A. Kovalevsky, L. Coates, A.A. Golosov, Inhibitor binding influences the protonation states of histidines in SARS-CoV-2 main protease, Chem. Sci. 12 (2021) 1513–1527.

[21] H.A. Alhadrami, A.M. Sayed, A.M. Sharif, E.I. Azhar, M.E. Rateb, Olive-derived triterpenes suppress SARS COV-2 main protease: a promising scaffold for future therapeutics, Molecules 26 (2021) 2654.

[22] H.-P. Chang, C.-Y. Chou, G.-G. Chang, Reversible unfolding of the severe acute respiratory syndrome coronavirus main protease in guanidinium chloride, Biophys. J. 92 (2007) 1374–1383.

[23] Q.A. Zhou, J. Kato-Weinstein, Y. Li, Y. Deng, R. Granet, L. Garner, C. Liu, D. Polshakov, C. Gessner, S. Watkins, Potential therapeutic agents and associated bioassay data for COVID-19 and related human coronavirus infections, ACS Pharmacol. Transl. Sci. 3 (2020) 813–834.

[24] D.W. Kneller, H. Li, G. Phillips, K.L. Weiss, Q. Zhang, M.A. Arnould, C.B. Jonsson, S. Surendranathan, J. Parvathareddy, M.P. Blakeley, Covalent narlaprevir- and boceprevir-derived hybrid inhibitors of SARS-CoV-2 main protease, Nat. Commun. 13 (2022) 2268.

[25] L. Zhang, D. Lin, X. Sun, U. Curth, C. Drosten, L. Sauerhering, S. Becker, K. Rox, R. Hilgenfeld, Crystal structure of SARS-CoV-2 main protease provides a basis for design of improved α-ketoamide inhibitors, Science 368 (2020) 409–412.

[26] H. Berg, M.A. Wirtz Martin, N. Altincekic, I. Alshamleh, J. Kaur Bains, J. Blechar, B. Ceylan, V. de Jesus, K. Dhamotharan, C. Fuks, S.L. Gande, B. Hargittay, K. F. Hohmann, M.T. Hutchison, S.M. Korn, R. Krishnathas, F. Kutz, V. Linhard, T. Matzel, N. Meiser, A. Niesteruk, D.J. Pyper, L. Schulte, S. Trucks, K. Azzaoui, M. J.J. Blommers, Y. Gadiya, R. Karki, A. Zaliani, P. Gribbon, M. da Silva Almeida, C. D. Anobom, A.L. Bula, M. Bütikofer, Í.P. Caruso, I.C. Felli, A.T. Da Poian, G. Cardoso de Amorim, N.K. Fourkiotis, A. Gallo, D. Ghosh, F. Gomes-Neto, O. Gorbatyuk, B. Hao, V. Kurauskas, L. Lecoq, Y. Li, N.C. Mebus-Antunes, M. Mompeán, T.C. Neves-Martins, M. Ninot-Pedrosa, A.S. Pinheiro, L. Pontoriero, Y. Pustovalova, R. Riek, A.J. Robertson, M.J. Abi Saad, M.Á. Treviño, A.C. Tsika, F. C.L. Almeida, A. Bax, K. Henzler-Wildman, J.C. Hoch, K. Jaudzems, D.V. Laurents, J. Orts, R. Pierattelli, G.A. Spyroulias, E. Duchardt-Ferner, J. Ferner, B. Fürtig, M. Hengesbach, F. Löhr, N. Qureshi, C. Richter, K. Saxena, A. Schlundt, S. Sreeramulu, A. Wacker, J.E. Weigand, J. Wirmer-Bartoschek, J. Wöhnert, H. Schwalbe, Comprehensive fragment screening of the SARS-CoV-2 proteome explores novel chemical space for drug development, Angew. Chem. Int. Ed. 134 (2022), e202205858.

[27] B. Tan, R. Joyce, H. Tan, Y. Hu, J. Wang, SARS-CoV-2 main protease drug design, assay development, and drug resistance studies, Acc. Chem. Res. 56 (2022) 157–168.

[28] A.K. Ghosh, J.L. Mishevich, A. Mesecar, H. Mitsuya, Recent drug development and medicinal chemistry approaches for the treatment of SARS-CoV-2 infection and COVID-19, ChemMedChem 17 (2022), e202200440.

[29] Y.F. Hallock, K.P. Manfredi, J.W. Blunt, J.H. Cardellina II, M. Schäffer, K.-P. Gulden, G. Bringmann, A.Y. Lee, J. Clardy, G. François, M.R. Boyd, Korupensamines A-D, novel antimalarial alkaloids from *Ancistrocladus korupensis*, J. Org. Chem. 59 (1994) 6349–6355.

[30] B.K. Lombe, D. Feineis, G. Bringmann, Dimeric naphthylisoquinoline alkaloids: polyketide-derived axially chiral bioactive quateraryls, Nat. Prod. Rep. 36 (2019) 1513–1545.

[31] N. Tajuddeen, G. Bringmann, *N,C*-Coupled naphthylisoquinoline alkaloids: a versatile new class of axially chiral natural products, Nat. Prod. Rep. 38 (2021) 2154–2186.

[32] D. Feineis, G. Bringmann, in: A.D. Kinghorn, H. Falk, S. Gibbons, Y. Asakawa, J.-K. Liu, V.M. Dirsch (Eds.), Asian *Ancistrocladus* lianas as creative producers of naphthylisoquinoline alkaloids, in: Progress in the Chemistry of Organic Natural Products, vol. 119, Springer, Cham, Heidelberg, New York, Dordrecht, London, 2023, pp. 1–335.

[33] G. Bringmann, C. Günther, M. Ochse, O. Schupp, S. Tasler, in: W. Herz, H. Falk, G. W. Kirby, R.E. Moore (Eds.), Biaryls in nature: a multi-facetted class of stereochemically, biosynthetically, and pharmacologically intriguing secondary

metabolites, in: Progress in the Chemistry of Organic Natural Products, vol. 82, Springer-Verlag, Wien, New York, 2001, pp. 1–249.
[34] G. Bringmann, T. Gulder, T.A.M. Gulder, M. Breuning, Atroposelective total synthesis of axially chiral biaryl natural products, Chem. Rev. 111 (2011) 563–639.
[35] N. Tajuddeen, D. Feineis, H. Ihmels, G. Bringmann, The stereoselective total synthesis of axially chiral naphthylisoquinoline alkaloids, Acc. Chem. Res. 55 (2022) 2370–2383.
[36] G. François, G. Timperman, W. Eling, L. Aké Assi, J. Holenz, G. Bringmann, Naphthylisoquinoline alkaloids against malaria: evaluation of the curative potentials of dioncophylline C and dioncopeltine A against *Plasmodium berghei* in vivo, Antimicrob. Agents Chemother. 41 (1997) 2533–2539.
[37] D.G.I. Kingston, M.B. Cassera, in: A.D. Kinghorn, H. Falk, S. Gibbons, Y. Asakawa, J.-K. Liu, V.M. Dirsch (Eds.), Antimalarial natural products, in: Progress in the Chemistry of Organic Natural Products, vol. 117, Springer Nature Switzerland AG, Cham, Switzerland, 2022, pp. 1–106.
[38] N. Tajuddeen, F.R. Van Heerden, Antiplasmodial natural products: an update, Malar. J. 18 (2019) 404.
[39] P. Moyo, W. Shamburger, M.E. van der Watt, J. Reader, A.C.C. De Sousa, T.J. Egan, V.J. Maharaj, G. Bringmann, L.-M. Birkholtz, Naphthylisoquinoline alkaloids, validated as hit multistage antiplasmodial natural products, Int. J. Parasitol. Drugs Drug Resist. 13 (2020) 51–58.
[40] B.K. Lombe, T. Bruhn, D. Feineis, V. Mudogo, R. Brun, G. Bringmann, Antiprotozoal spirombandakamines $A_1$ and $A_2$, fused naphthylisoquinoline dimers from a Congolese *Ancistrocladus* plant, Org. Lett. 19 (2017) 6740–6743.
[41] A. Ponte-Sucre, J.H. Faber, T. Gulder, I. Kajahn, S.E.H. Pedersen, M. Schultheis, G. Bringmann, H. Moll, Activities of naphthylisoquinoline alkaloids and synthetic analogs against *Leishmania major*, Antimicrob. Agents Chemother. 51 (2007) 188–194.
[42] A. Ponte-Sucre, T. Gulder, A. Wegehaupt, C. Albert, C. Rikanović, L. Schaeflein, A. Frank, M. Schultheis, M. Unger, U. Holzgrabe, G. Bringmann, H. Moll, Structure–activity relationship and studies on the molecular mechanism of leishmanicidal *N,C*-coupled arylisoquinolinium salts, J. Med. Chem. 52 (2009) 626–636.
[43] A. Ponte-Sucre, T. Gulder, T.A.M. Gulder, G. Vollmers, G. Bringmann, H. Moll, Alterations to the structure of *Leishmania major* induced by *N*-arylisoquinolines correlate with compound accumulation and disposition, J. Med. Microbiol. 59 (2010) 69–75.
[44] A. Cecil, C. Rikanović, K. Ohlsen, C. Liang, J. Bernhardt, T.A. Oelschlaeger, T. Gulder, G. Bringmann, U. Holzgrabe, M. Unger, T. Dandekar, Modeling antibiotic and cytotoxic effects of the dimeric isoquinoline IQ-143 on metabolism and its regulation in *Staphylococcus aureus, Staphylococcus epidermidis* and human cells, Genome Biol. 12 (2011) R24.
[45] G. François, M. van Looveren, G. Timperman, B. Chimanuka, L. Aké Assi, J. Holenz, G. Bringmann, Larvicidal activity of the naphthylisoquinoline alkaloid dioncophylline A against the malaria vector *Anopheles stephensi*, J. Ethnopharmacol. 54 (1996) 125–130.
[46] G. Bringmann, J. Holenz, L. Aké Assi, C. Zhao, K. Hostettmann, Molluscicidal activity of naphthylisoquinoline alkaloids from *Triphyophyllum* and *Ancistrocladus* species, Planta Med. 62 (1996) 556–557.
[47] G. Bringmann, J. Holenz, L. Aké Assi, K. Hostettmann, Molluscicidal activity (*Biomphalaria glabrata*) of dioncophylline A: structure-activity investigations, Planta Med. 64 (1998) 485–486.
[48] G. Bringmann, S. Gramatzki, C. Grimm, P. Proksch, Feeding deterrency and growth retarding activity of the naphthylisoquinoline alkaloid dioncophylline A against *Spodoptera littoralis*, Phytochemistry 31 (1992) 3821–3825.
[49] G. Bringmann, J. Holenz, B. Wiesen, B.W. Nugroho, P. Proksch, Dioncophylline A as a growth-retarding agent against the herbivorous insect *Spodoptera littoralis*: structure–activity relationships, J. Nat. Prod. 60 (1997) 342–347.
[50] G. Bringmann, S. Fayez, W. Shamburger, D. Feineis, S. Winiarczyk, R. Janecki, Ł. Adaszek, Naphthylisoquinoline alkaloids and their synthetic analogs as potent novel inhibitors against *Babesia canis in vitro*, Vet. Parasitol. 283 (2020), 109177.
[51] J. Li, R. Seupel, D. Feineis, V. Mudogo, M. Kaiser, R. Brun, D. Brünnert, M. Chatterjee, E.J. Seo, T. Efferth, G. Bringmann, Dioncophyllines $C_2$, $D_2$, and F and related naphthylisoquinoline alkaloids from the Congolese liana *Ancistrocladus ileboensis* with potent activities against *Plasmodium falciparum* and against multiple myeloma and leukemia cell lines, J. Nat. Prod. 80 (2017) 443–458.
[52] S. Awale, D.F. Dibwe, C. Balachandran, S. Fayez, D. Feineis, B.K. Lombe, G. Bringmann, Ancistrolikokine $E_3$, a 5,8′-coupled naphthylisoquinoline alkaloid, eliminates the tolerance of cancer cells to nutrition starvation by inhibition of the Akt/mTOR/autophagy signaling pathway, J. Nat. Prod. 81 (2018) 2282–2291.
[53] S. Fayez, T. Bruhn, D. Feineis, L. Aké Assi, S. Awale, G. Bringmann, Ancistrosecolines A-F, unprecedented *seco*-naphthylisoquinoline alkaloids from the roots of *Ancistrocladus abbreviatus*, with apoptosis-inducing potential against HeLa cancer cells, J. Nat. Prod. 83 (2020) 1139–1151.
[54] S. Fayez, A. Cacciatore, S. Sun, M. Kim, L. Aké Assi, D. Feineis, S. Awale, G. Bringmann, Ancistrobrevidines A-C and related naphthylisoquinoline alkaloids with cytotoxic activities against HeLa and pancreatic cancer cells, from the liana *Ancistrocladus abbreviatus*, Bioorg. Med. Chem. 30 (2021), 115950.
[55] P.P. Kushwaha, A.K. Singh, K.S. Prajapati, M. Shuaib, S. Fayez, G. Bringmann, S. Kumar, Induction of apoptosis in breast cancer cells by naphthylisoquinoline alkaloids, Toxicol. Appl. Pharmacol. 409 (2020), 115297.
[56] M.R. Boyd, Y.F. Hallock, J.H. Cardellina II, K.P. Manfredi, J.W. Blunt, J. B. McMahon, R.W. Buckheit Jr., G. Bringmann, M. Schäffer, G.M. Cragg, D. W. Thomas, J.G. Jato, Anti-HIV michellamines from *Ancistrocladus korupensis*, J. Med. Chem. 37 (1994) 1740–1745.
[57] K.P. Manfredi, J.W. Blunt, J.H. Cardellina II, J.B. McMahon, L.L. Pannell, G. M. Cragg, M.R. Boyd, Novel alkaloids from the tropical plant *Ancistrocladus abbreviatus* inhibit cell killing by HIV-1 and HIV-2, J. Med. Chem. 34 (1991) 3402–3405.
[58] J.B. McMahon, M.J. Currens, R.J. Gulakowski, R.W. Buckheit Jr., C. Lackman-Smith, Y.F. Hallock, M.R. Boyd, Michellamine B, a novel plant alkaloid, inhibits human immunodeficiency virus-induced cell killing by at least two distinct mechanisms, Antimicrob. Agents Chemother. 39 (1995) 484–488.
[59] G. Bringmann, C. Steinert, D. Feineis, V. Mudogo, J. Betzin, C. Scheller, HIV-inhibitory michellamine-type dimeric naphthylisoquinoline alkaloids from the Central African liana *Ancistrocladus congolensis*, Phytochemistry 128 (2016) 71–81.
[60] H.A. Alhadrami, A.M. Sayed, H.M. Hassan, K.A. Youssif, Y. Gaber, Y. Moatasim, O. Kutkat, A. Mostafa, M.A. Ali, M.E. Rateb, U.R. Abdelmohsen, N.M. Gamaleldin, Cnicin as an anti-SARS-CoV-2: an integrated in silico and in vitro approach for the rapid identification of potential COVID-19 therapeutics, Antibiotics 10 (2021) 542.
[61] H.A. Alhadrami, G. Burgio, B. Thissera, R. Orfali, S.E. Jiffri, M. Yaseen, A.M. Sayed, M.E. Rateb, Neoechinulin A as a promising SARS-CoV-2 $M^{pro}$ inhibitor: in vitro and in silico study showing the ability of simulations in discerning active from inactive enzyme inhibitors, Mar. Drugs 20 (2022) 163.
[62] M.H. ElNaggar, G.M. Abdelwahab, O. Kutkat, M. GabAllah, M.A. Ali, M.E.A. El-Metwally, A.M. Sayed, U.R. Abdelmohsen, A.T. Khalil, Aurasperone A inhibits SARS CoV-2 in vitro: an integrated in vitro and in silico study, Mar. Drugs 20 (2022) 179.
[63] R. Orfali, M.E. Rateb, H.M. Hassan, M. Alonazi, M.R. Gomaa, N. Mahrous, M. GabAllah, A. Kandeil, S. Perveen, U.R. Abdelmohsen, A.M. Sayed, Sinapic acid suppresses SARS CoV-2 replication by targeting its envelope protein, Antibiotics 10 (2021) 420.
[64] R.A. Eid, M.O. Elgendy, A.O. El-Gendy, S.O. Elgendy, L. Belbahri, A.M. Sayed, M. E. Rateb, Efficacy of ceftazidime and cefepime in the management of COVID-19 patients: single center report from Egypt, Antibiotics 10 (2021) 1278.
[65] G. Sandeep, K.P. Nagasree, M. Hanisha, M.M.K. Kumar, AUDocker LE: A GUI for virtual screening with AUTODOCK Vina, BMC Res. Notes 4 (2011) 1–4.
[66] H. Su, S. Yao, W. Zhao, Y. Zhang, J. Liu, Q. Shao, Q. Wang, M. Li, H. Xie, W. Shang, Identification of pyrogallol as a warhead in design of covalent inhibitors for the SARS-CoV-2 3CL protease, Nat. Commun. 12 (2021) 1–12.
[67] A. Clyde, S. Galanie, D.W. Kneller, H. Ma, Y. Babuji, B. Blaiszik, A. Brace, T. Brettin, K. Chard, R. Chard, High-throughput virtual screening and validation of a SARS-CoV-2 main protease noncovalent inhibitor, J. Chem. Inf. Model. 62 (2021) 116–128.
[68] S.T. Ngo, N.M. Tam, M.Q. Pham, T.H. Nguyen, Benchmark of popular free energy approaches revealing the inhibitors binding to SARS-CoV-2 $M^{pro}$, J. Chem. Inf. Model. 61 (2021) 2302–2312.
[69] F. Colizzi, R. Perozzo, L. Scapozza, M. Recanatini, A. Cavalli, Single-molecule pulling simulations can discern active from inactive enzyme inhibitors, J. Am. Chem. Soc. 132 (2010) 7361–7371.
[70] C. Ma, M.D. Sacco, B. Hurst, J.A. Townsend, Y. Hu, T. Szeto, X. Zhang, B. Tarbet, M.T. Marty, Y. Chen, J. Wang, Boceprevir, GC-376, and calpain inhibitors II, XII inhibit SARS-CoV-2 viral replication by targeting the viral main protease, Cell Res. 30 (2020) 678–692.
[71] S. Fayez, D. Feineis, V. Mudogo, S. Awale, G. Bringmann, Ancistrolikokines E–H and related 5,8′-coupled naphthylisoquinoline alkaloids from the Congolese liana *Ancistrocladus likoko* with antiausterity activities against PANC-1 human pancreatic cancer cells, RSC Adv. 7 (2017) 53740–53751.
[72] S. Fayez, D. Feineis, L. Aké Assi, M. Kaiser, R. Brun, S. Awale, G. Bringmann, Ancistrobrevines E-J and related naphthylisoquinoline alkaloids from the West African liana *Ancistrocladus abbreviatus* with inhibitory activities against *Plasmodium falciparum* and PANC-1 human pancreatic cancer cells, Fitoterapia 131 (2018) 245–259.
[73] G. Bringmann, M. Rübenacker, J.R. Jansen, D. Scheutzow, L. Aké Assi, On the structure of the Dioncophyllaceae alkaloids dioncophylline A ("triphyophylline") and "*O*-methyl-triphyophylline", Tetrahedron Lett. 31 (1990) 639–642.
[74] G. Bringmann, M. Rübenacker, P. Vogt, H. Busse, L. Aké Assi, K. Peters, H.G. von Schnering, Dioncopeltine A and dioncolactone A: alkaloids from *Triphyophyllum peltatum*, Phytochemistry 30 (1991) 1691–1696.
[75] G. Bringmann, F. Teltschik, M. Schäffer, R. Haller, S. Bär, S.A. Robertson, M. A. Isahakia, Ancistrobertsonine A and related naphthylisoquinoline alkaloids from *Ancistrocladus robertsoniorum*, Phytochemistry 47 (1998) 31–35.
[76] G. Bringmann, M. Rübenacker, R. Weirich, L. Aké Assi, Dioncophylline C from the roots of *Triphyophyllum peltatum*, the first 5,1′-coupled Dioncophyllaceae alkaloid, Phytochemistry 31 (1992) 4019–4024.
[77] G. Bringmann, M. Ochse, R. Götz, First atropo-divergent total synthesis of the antimalarial korupensamines A and B by the "lactone method", J. Org. Chem. 65 (2000) 2069–2077.
[78] G.M. Morris, R. Huey, W. Lindstrom, M.F. Sanner, R.K. Belew, D.S. Goodsell, A. J. Olson, AutoDock4 and AutoDockTools4: automated docking with selective receptor flexibility, J. Comput. Chem. 30 (2009) 2785–2791.
[79] P. Eastman, J. Swails, J.D. Chodera, R.T. McGibbon, Y. Zhao, K.A. Beauchamp, L. P. Wang, A.C. Simmonett, M.P. Harrigan, C.D. Stern, R.P. Wiewiora, OpenMM 7: rapid development of high performance algorithms for molecular dynamics, PLoS Comput. Biol. 13 (2017), e1005659.
[80] D. Seeliger, B.L. de Groot, Ligand docking and binding site analysis with PyMOL and Autodock/Vina, J. Comput. Aided Mol. Des. 24 (2010) 417–422.
[81] S. Dallakyan, A.J. Olson, Small-molecule library screening by docking with PyRx in, in: J. Hempel, C. Williams, C. Hong (Eds.), Chemical Biology. Methods in Molecular Biology vol. 1263, Humana Press, New York, 2015, pp. 243–250.

[82] H.A. Alhadrami, A.M. Sayed, H. Al-Khatabi, N.A. Alhakamy, M.E. Rateb, Scaffold hopping of α-rubromycin enables direct access to FDA-approved cromoglicic acid as a SARS-CoV-2 $M^{Pro}$ inhibitor, Pharmaceuticals 14 (2021) 541.
[83] Y. Miao, J.A. McCammon, Gaussian accelerated molecular dynamics: theory, implementation, and applications, Annu. Rep. Comput. Chem. 13 (2017) 231–278.
[84] M. Zimniak, L. Kirschner, H. Hilpert, N. Geiger, O. Danov, H. Oberwinkler, M. Steinke, K. Sewald, J. Seibel, J. Bodem, The serotonin reuptake inhibitor fluoxetine inhibits SARS-CoV-2 in human lung tissue, Sci. Rep. 11 (2021) 5890.
[85] N. Geiger, L. Kersting, J. Schlegel, L. Stelz, S. Fähr, V. Diesendorf, V. Roll, M. Sostmann, E.M. König, S. Reinhard, D. Brenner, S. Schneider-Schaulies, M. Sauer, J. Seibel, J. Bodem, The acid ceramidase is a SARS-CoV-2 host factor, Cells 11 (2022) 2532.